A Common Base Mode of Asian Summer Monsoon Variability across Timescales

XUDONG WANG,[a,b] SHANG-PING XIE,[b] ZHAOYONG GUAN,[a] AND MINYANG WANG[b,c,d]

[a] *Collaborative Innovation Center on Forecast and Evaluation of Meteorological Disaster/KLME/ILCEC, Nanjing University of Information Science and Technology, Nanjing, China*
[b] *Scripps Institution of Oceanography, University of California San Diego, La Jolla, California*
[c] *State Key Laboratory of Tropical Oceanography, South China Sea Institute of Oceanology, Chinese Academy of Sciences, Guangzhou, China*
[d] *University of Chinese Academy of Sciences, Beijing, China*

(Manuscript received 9 November 2020, in final form 7 June 2021)

ABSTRACT: The summer intraseasonal oscillation (ISO) is characterized by a northward-moving rainband in the Indo–western Pacific warm pool region. The physical origin of the ISO is not fully understood, as it is masked by strong interaction of convection and circulation. This study examines intraseasonal to interannual variability during June–August over the Indo–western Pacific warm pool region. The results show that the tropical northwest Pacific anomalous anticyclone (NWP-AAC) is a fundamental mode on both intraseasonal and interannual time scales, destabilized by the monsoon mean state, specifically through barotropic energy conversion and convective feedback in the low-level confluence between the monsoon westerlies and easterly trade winds. On the interannual time scale, the NWP-AAC shows a biennial tendency, reversing phase from the summer of El Niño to the summer that follows; the AAC in post–El Niño summer is excited indirectly through sea surface temperature anomalies in the Indo–NWP. On the intraseasonal time scale, the column-integrated moisture advection causes the NWP-AAC-related convection to propagate northward. Our results provide a unifying view of multiscale Asian summer monsoon variability, with important implications for subseasonal to seasonal prediction.

KEYWORDS: ENSO; Madden-Julian oscillation; Monsoons; Air-sea interaction

1. Introduction

Summer is the rainy season for the Asian monsoon region, which encompasses much of South, Southeast, and East Asia, home to more than 3 billion people. The Asian summer monsoon exhibits pronounced variability on a wide range of time scales from intraseasonal to interannual. El Niño–Southern Oscillation (ENSO) is the major driver of interannual variability. It develops in boreal summer, peaks in winter, and decays rapidly in the following spring. An ENSO event affects the Asian monsoon during the summer when the coupled phenomenon develops and the summer of the following year. The concurrent El Niño effect on the Asian summer monsoon includes the Southern Oscillation, reduced rainfall over India (Webster and Yang 1992), and the weakened Walker circulation in favor of the Indian Ocean dipole (IOD) mode (Saji et al. 1999).

A large-scale anomalous anticyclone (AAC) spanning from the north Indian Ocean to the northwest Pacific (NWP) is a recurrent low-level circulation pattern that tends to take place in post–El Niño summers (Wang et al. 2003; Xie et al. 2009) when equatorial eastern Pacific sea surface temperature (SST) anomalies have largely dissipated (Xie et al. 2016). Ocean–atmosphere coupling plays critical roles in enabling the AAC to persist into the following summer. During post–El Niño summer, the El Niño–induced tropical Indian Ocean warming excites a warm tropospheric Kelvin wave propagating into the western Pacific. The associated boundary layer Ekman divergence in the NWP suppresses convection and triggers AAC in this region (Xie et al. 2009). The SST cooling in the NWP also favors the AAC through the atmospheric Rossby wave response (Wang et al. 2003; Wu et al. 2010). The Indo–western Pacific Ocean capacitor (IPOC) mode refers to the above coherent coupled anomalies over the tropical Indo–NWP in post–El Niño summers (Xie et al. 2016). While the IPOC is closely related to ENSO, recent model and observational studies show that regional ocean–atmosphere interaction can produce the IPOC without ENSO forcing as in 2020 (Zhou et al. 2021; Wang et al. 2018; C. Wang et al. 2020). Using the atmospheric general circulation model (AGCM) forced by climatological SST, the leading interannual mode in the summer Indo–NWP is shown to feature an AAC pattern (Zhou et al. 2018). This AAC pattern should be an atmospheric internal mode that is white on the interannual time scale. This suggests that the AAC can be generated without ocean coupling. Indeed, Hu et al. (2019) and X. Wang et al. (2020) showed that the instability of the low-level mean flow over the Indo–NWP energizes the AAC.

The Madden–Julian oscillation (MJO) (Madden and Julian 1971, 1972) and its summer counterpart, the intraseasonal oscillation (ISO), are the dominant modes of tropical intraseasonal variability. The MJO exhibits an envelope of enhanced deep convection several thousand kilometers across

Supplemental information related to this paper is available at the Journals Online website: https://doi.org/10.1175/JCLI-D-20-0856.s1.

Corresponding author: Zhaoyong Guan, guanzy@nuist.edu.cn

DOI: 10.1175/JCLI-D-20-0856.1

that travels eastward at approximately $5\,m\,s^{-1}$ during boreal winter, coupled with the planetary-scale waves in the tropics. The MJO strongly modulates the monsoon systems (Joseph et al. 2009; Pohl and Camberlin 2006; Lorenz and Hartmann 2006; Grimm 2019), tropical cyclones (Frank and Roundy 2006), ENSO (McPhaden 1999; Moore and Kleeman 1999), and extreme events including droughts, flooding, and heat waves (Zhang 2013). The MJO/ISO exhibits pronounced seasonality in its propagation characteristics. The MJO is active and broadly symmetric along the equator during boreal winter. During boreal summer, in contrast, the ISO shows a marked poleward propagation in addition to the eastward propagation (Adames et al. 2016; Jiang et al. 2018). Recently, the moisture mode theory (Sobel and Maloney 2012, 2013; Adames and Kim 2016) has been proposed to explain the propagation and growth characteristics of the MJO/ISO. An important finding of the moisture mode theory is that the horizontal advection of column-integrated moist static energy (MSE) plays an important role in driving the eastward (northward) propagation of the winter MJO (summer ISO; Adames and Kim 2016; Jiang et al. 2018). The summer ISO has far-reaching effects on western hemispheric hurricanes (Maloney and Hartmann 2000) by radiating the equatorial Kelvin wave (Small et al. 2011) and the North American monsoon via the tropospheric Rossby wave teleconnection (Jiang and Lau 2008).

While the summer ISO and the interannual Indo–NWP AAC have each been studied extensively, their interactions are poorly understood. Our recent research (X. Wang et al. 2020) showed that the monthly average of ISO anomalies contributes to interannual variability, with a strong projection onto the Indo–NWP AAC pattern. This hints at a strong upscale energy cascade from the ISO to the interannual AAC. This cross-scale interaction is important during the 2016 summer following a major El Niño (X. Wang et al. 2020).

This study explores the tantalizing possibility that the AAC is a fundamental summer mode of the Indo–NWP region through which cross-timescale interactions occur. The remote El Niño forcing excites this mode, which is additionally energized by barotropic energy conversion in the climatological monsoon–trade wind confluence zone and convective feedback. We show that on the intraseasonal time scale, the monsoon flow and climatological column-integrated moisture distribution are such that the NWP-AAC mode induces a northeastward propagation, in support of the moisture mode theory.

The rest of the paper is organized as follows. Section 2 describes the data and methods. Section 3 presents the results and section 4 summarizes and discusses our results.

2. Data and methods

a. Datasets

We use the daily wind velocity, precipitation, temperature, and specific humidity from the European Centre for Medium-Range Weather Forecasts interim reanalysis (ERA-Interim; Dee et al. 2011) with a horizontal resolution of $1.5° \times 1.5°$. The CPC Merged Analysis of Precipitation (CMAP) pentad data (Xie and Arkin 1997) are also used in comparison with the ERA-Interim precipitation.

b. Methodology

To evaluate the intraseasonal and interannual variability together, we apply the 20-day Lanczos low-pass filter (Duchon 1979) after removing the climatological daily mean over the whole period (1979–2017) and utilize the low-pass filtered data during 1 June–31 August. Key features of the ISO including the phase propagation remain unchanged, compared to the traditional 20–100-day bandpass filter following the removal of the climatological daily mean, seasonal mean, or first three harmonics of annual cycle (Lee et al. 2013).

For the summer ISO, we conduct an empirical orthogonal function (EOF) analysis of normalized 20-day low-pass filtered daily upper (200 hPa) and low-level (850 hPa) tropospheric wind anomalies in the Indo–NWP domain (10°S–25°N, 40°–140°E) from June to August over the 39-yr period 1979–2017. We compared with the boreal summer intraseasonal oscillation (BSISO) indices of Lee et al. (2013), derived from the first two leading multivariate EOFs of outgoing longwave radiation (OLR) and 850-hPa zonal wind anomalies in the Asian summer monsoon region. Our EOF modes are almost identical to the BSISO modes and capture a more robust northward propagation than real-time multivariate MJO (RMM) indices (Wheeler and Hendon 2004).

The vertically integrated moisture budget equation is approximately given as

$$\left\langle \frac{\partial q}{\partial t} \right\rangle = -\langle \mathbf{V} \cdot \nabla q \rangle - \left\langle \omega \frac{\partial q}{\partial p} \right\rangle - P + E, \tag{1}$$

where P and E are precipitation and surface evaporation, respectively, $\mathbf{V} \equiv (u, v)$ is the horizontal velocity vector, ω is the vertical pressure velocity, and q is the specific humidity. The angle brackets represent vertical integrals from 1000 to 100 hPa. Variables in Eq. (1) are further broken into (using specific humidity as an example)

$$q = \overline{q} + q' + q'',$$

where the overbar, prime, and double prime denote the seasonal mean, ISO-related, and higher-frequency (time scale shorter than 20 days) variability, respectively. The horizontal moisture advection term in Eq. (1) can be further written as

$$-\langle \mathbf{V} \cdot \nabla q \rangle' \approx -\langle \overline{\mathbf{V}} \cdot \nabla q' \rangle - \langle \mathbf{V}' \cdot \nabla \overline{q} \rangle - \langle \mathbf{V}' \cdot \nabla q' \rangle' - \langle \mathbf{V}'' \cdot \nabla q'' \rangle'. \tag{2}$$

The first term on the right-hand side describes the horizontal advection of intraseasonal moisture by the background winds, the second term is the advection of seasonal mean moisture by the intraseasonal winds, the third term represents the advection of intraseasonal moisture by the intraseasonal winds, and the fourth term is the nonlinear advection of synoptic eddies.

Following Hoskins et al. (1983), we evaluate barotropic conversion (CK) of kinetic energy from the climatological mean flow (denoted by overbar) into monthly anomalies (prime),

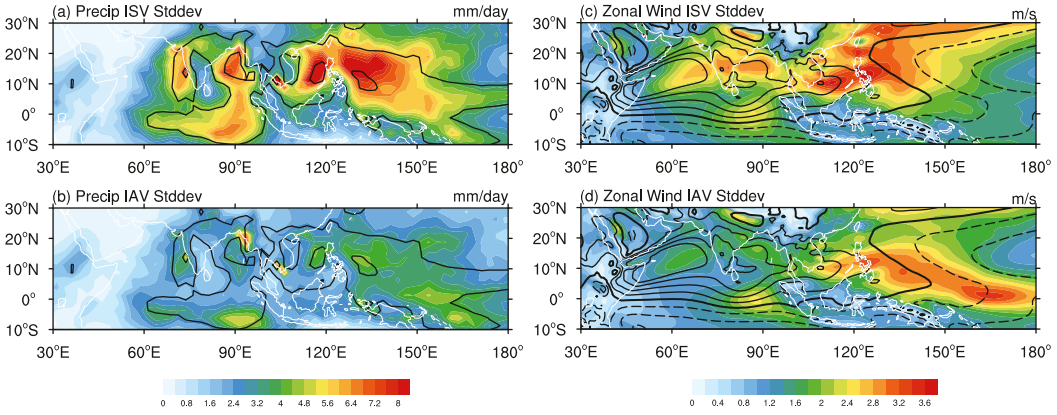

FIG. 1. (a) Intraseasonal and (b) interannual standard deviations of CMAP rainfall (shading; units: mm day^{-1}) over the Indo–NWP region. (c),(d) Intraseasonal and interannual standard deviations, respectively, for the ERA-Interim zonal wind at 850 hPa (shading, units: m s^{-1}). Black contours in (a) and (b) represent climatological rainfall exceeds 7 mm day^{-1}. Contours in (c) and (d) show the climatological westerlies (solid line) and easterlies (dashed line) at intervals of 4 m s^{-1}.

$$\frac{\partial \mathrm{KE}}{\partial t} = \underbrace{\frac{\overline{v'^2}-\overline{u'^2}}{2}\left(\frac{\partial \overline{u}}{\partial x}-\frac{\partial \overline{v}}{\partial y}\right)-\overline{u'v'}\left(\frac{\partial \overline{u}}{\partial y}+\frac{\partial \overline{v}}{\partial x}\right)}_{\mathrm{CK}} - \underbrace{\overline{\mathbf{V}}\cdot\nabla(\mathrm{KE})}_{\mathrm{KA}} - \underbrace{\mathbf{V}'\cdot\nabla(\mathrm{KE})}_{} - \underbrace{\frac{R}{p}\overline{\omega' T'}}_{\mathrm{KP}} - \underbrace{\nabla\cdot\left(\overline{\mathbf{V}'\Phi'}\right)}_{\mathrm{KZ}} + \mathrm{KR} \tag{3}$$

and

$$\mathrm{CK} \equiv \frac{\overline{v'^2}-\overline{u'^2}}{2}\left(\frac{\partial \overline{u}}{\partial x}-\frac{\partial \overline{v}}{\partial y}\right)-\overline{u'v'}\left(\frac{\partial \overline{u}}{\partial y}+\frac{\partial \overline{v}}{\partial x}\right)$$

at the 850-hPa level. The positive CK means that eddy kinetic energy (KE), defined as $(\overline{u'^2}+\overline{v'^2})/2$, is converted from the mean flow. The terms KA, KP, KZ, and KR, representing redistribution of KE by circulations, eddy available potential energy, and residuals, make small contributions to the local energetics (not shown).

Available potential energy [$\mathrm{APE} \equiv (R/pS_p)(T'^2/2)$] is converted from the climatological mean state to the monthly perturbations through baroclinic energy conversion (Kosaka and Nakamura 2006; Lau and Lau 1992):

$$\frac{\partial \mathrm{APE}}{\partial t} \approx \underbrace{-\frac{R}{pS_p}\left(\overline{u'T'}\frac{\partial \overline{T}}{\partial x}+\overline{v'T'}\frac{\partial \overline{T}}{\partial y}\right)}_{\mathrm{CP}} + \underbrace{\frac{R}{p}\overline{\omega' T'}}_{-\mathrm{KP}} + \underbrace{\frac{R}{pC_pS_p}\overline{T'Q'}}_{\mathrm{CQ}} \tag{4}$$

and

$$\mathrm{CP} \equiv -\frac{R}{pS_p}\left(\overline{u'T'}\frac{\partial \overline{T}}{\partial x}+\overline{v'T'}\frac{\partial \overline{T}}{\partial y}\right).$$

Here, $S_p \equiv (R/p)[(R\overline{T}/pC_p)-d\overline{T}/dp]$ is the mean static stability, R and C_p denote the gas constant and the specific heat, and T denotes the tropospheric temperature. Eddy APE generation by anomalous diabatic heating CQ is defined as

$$\mathrm{CQ} \equiv \frac{R}{pC_pS_p}\overline{T'Q'}, \tag{5}$$

where Q on the right-hand side denotes anomalous apparent heat source.

3. Results

a. Intraseasonal modes

We start by evaluating the intraseasonal (20–100 days) and interannual standard deviation of precipitation and zonal wind at 850 hPa over the Indo–NWP region (Fig. 1). Intraseasonal precipitation variability is largest over the western coast of India, Bay of Bengal, and NWP regions (Fig. 1a). The tropical southeastern Indian Ocean and equatorial western Pacific also exhibit strong intraseasonal precipitation variability. The interannual standard deviation of precipitation shows a similar pattern albeit with reduced magnitudes (Fig. 1b). Compared with the CMAP product, ERA-Interim rainfall shows biases in the western Bay of Bengal (not shown). Intraseasonal zonal wind is most pronounced in the NWP region, followed by the secondary peak in the Indian summer monsoon (ISM) region (Fig. 1c). Interannual zonal wind variability is enhanced over the tropical southeastern Indian Ocean and western equatorial Pacific near the international date line, related to the Indian Ocean dipole and ENSO, respectively. Both intraseasonal and interannual variability in zonal wind is high over the NWP (5°–20°N) where the monsoon westerlies and easterly trade winds meet (Figs. 1c,d). We will show that barotropic energy conversion gives rise to elevated variability in this broad confluence of the mean zonal wind.

We perform joint EOF analysis on wind velocity variability (u', v') at 850- and 200-hPa levels in the domain of 10°S–25°N, 40°–140°E. Here we use 20-day low-pass filtered data to retain

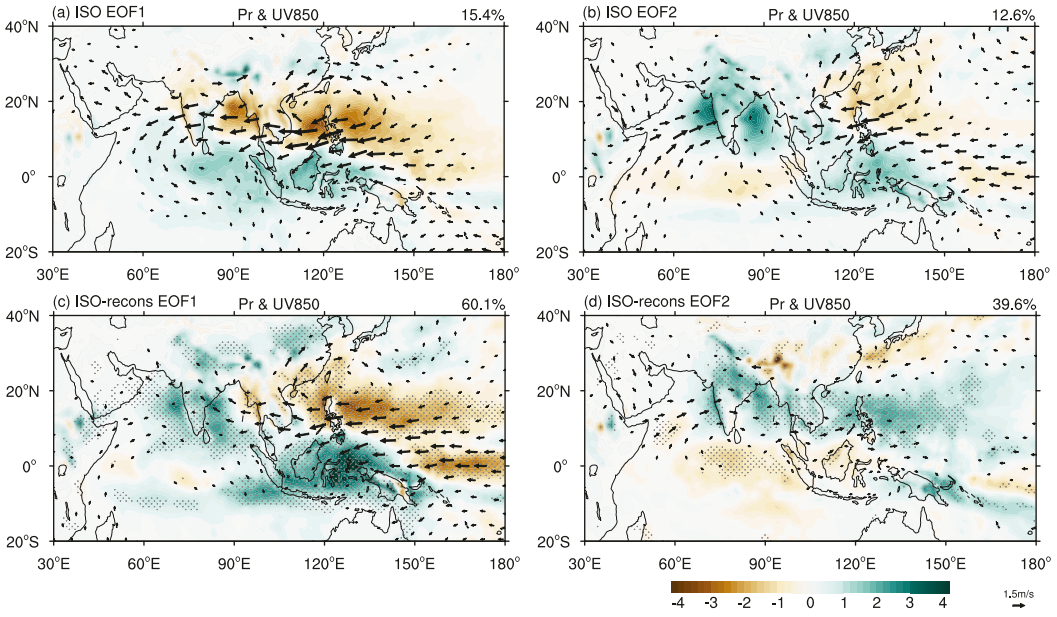

FIG. 2. (a),(b) Rainfall (shading) and 850-hPa wind (vectors) anomalies regressed onto the first two normalized ISO EOF PCs. (c),(d) Monthly anomalies regressed against the normalized monthly $PC_{1,2}^{rec}$. Stippling in (c) and (d) represents the rainfall anomalies > 99% confidence level, based upon the *t* test.

interannual variability. Since EOF modes using the 20–100-day bandpass data are nearly identical (section 2b), we will call the 20-day low-pass modes the ISO. Figures 2a and 2b show precipitation and 850-hPa wind anomalies regressed onto the first two EOF principal components (PCs) of summer ISO (ISO1 and ISO2). The ISO1 captures 15.4% of combined 850- and 200-hPa wind variance during summer with zonally elongated rainfall bands stacked in the meridional direction. Increased rainfall is located in the Maritime Continent through the western equatorial Indian Ocean, accompanied with a band of decreased rainfall from the Bay of Bengal through the South China Sea (Fig. 2a). Low-level wind anomalies show an anticyclone over the South China Sea to the NWP region, with easterly wind anomalies in the western Indian Ocean, related to the break of the ISM (Goswami and Mohan 2001; Annamalai and Slingo 2001). The ISO2 accounts for 12.6% of combined wind variance (Fig. 2b), with a northwest–southeast tilted rainband from the west coast of India to the Maritime Continent, accompanied with decreased precipitation over the NWP region. The ISO2 shows an anticyclone over the NWP that is zonally confined and displaced compared to the anticyclone in ISO1. The strengthened southwesterly in India associated with the ISO2 indicates the active phase of the ISM (Annamalai and Slingo 2001). The spatial pattern of two leading ISO EOF modes is almost identical to the boreal summer intraseasonal oscillation (BSISO) index 1 (Lee et al. 2013), although we use the 20-day low-pass filter instead of the traditional 20–100-day bandpass filter to extract the ISO. The PCs of ISO1 and ISO2, denoted as PC_1^{ISO} and PC_2^{ISO}, are mutually correlated at 0.39 with PC_1^{ISO} leading by 11 days (Fig. 3a). Note that PC_1^{ISO} and PC_2^{ISO} show greatest coherence at 30–40-day range with a 90° phase difference (Fig. 3b). The composite life cycle of summer ISO based upon PC_1^{ISO} and PC_2^{ISO} further proves that the 20-day low-pass filtered ISO mode pair well captures the propagating features of convection and circulation anomalies on the intraseasonal time scale (Fig. 4).

b. *Interannual modes*

ISO contributes to monthly mean anomalies over the Indo–NWP region (X. Wang et al. 2020). Here we reconstruct monthly anomalies (A^{rec}) from the first two ISO modes

$$A^{rec} = \overline{PC_1^{ISO}} \times EOF_1^{ISO} + \overline{PC_2^{ISO}} \times EOF_2^{ISO}, \qquad (6)$$

where the overbar denotes the month mean. The reconstruction explains 31% of the raw monthly low-level zonal wind variability in the domain of 10°S–25°N, 40°–140°E. Then, we perform an EOF analysis on reconstructed monthly-mean wind at 850 and 200 hPa:

$$A^{rec} = PC_1^{rec} \times EOF_1^{rec} + PC_2^{rec} \times EOF_2^{rec}, \qquad (7)$$

where EOF_i^{rec} represents the eigenmode of monthly anomalies for the summer season [June–August (JJA)], and PC_i^{rec} is the principal component that is $N_{yr} = 3 \times 39 = 117$ months long. EOF_1^{rec} explains 60.1% of total wind variance for the monthly mean from Eq. (7).

EOF_1^{rec} features a prominent low-level anticyclone over the NWP, accompanied with the easterly anomalies on its southern flank (Fig. 2c). Hereafter we refer to it as the NWP anomalous anticyclone (NWP-AAC) mode. Rainfall anomalies associated with the NWP-AAC in the Indo–NWP region shows a dipole with decreased rainfall over the NWP and enhanced rainfall in the Maritime Continent. The increased rainfall in India and its vicinity represents the impact of the NWP-AAC on ISM

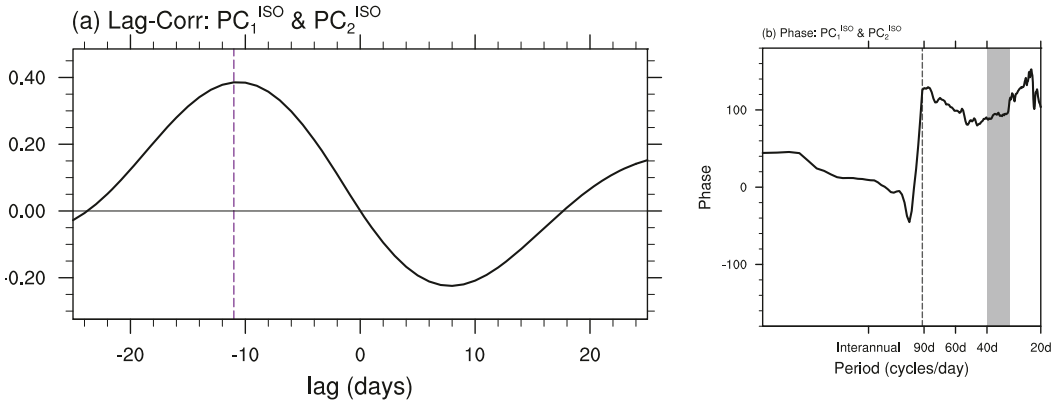

FIG. 3. (a) Lag correlations between the PC_1^{ISO} and PC_2^{ISO}. (b) Phase difference between the PC_1^{ISO} and PC_2^{ISO}.

rainfall (Mishra et al. 2012; Zhou et al. 2019). The PC_1^{rec} displays marked month-to-month persistence; the July mean PC of NWP-AAC is significantly correlated with both June and August values (Fig. 5). The temporal persistence suggests SST forcing effect.

ENSO is an important driver of the interannual NWP-AAC. The PC_1^{rec} is correlated with both subsequent and antecedent December–February (DJF) Niño-3.4 SST, respectively at −0.74 and 0.52. Figure 6 shows rainfall and 850-hPa wind anomalies during the El Niño and post–El Niño summers. Circulation

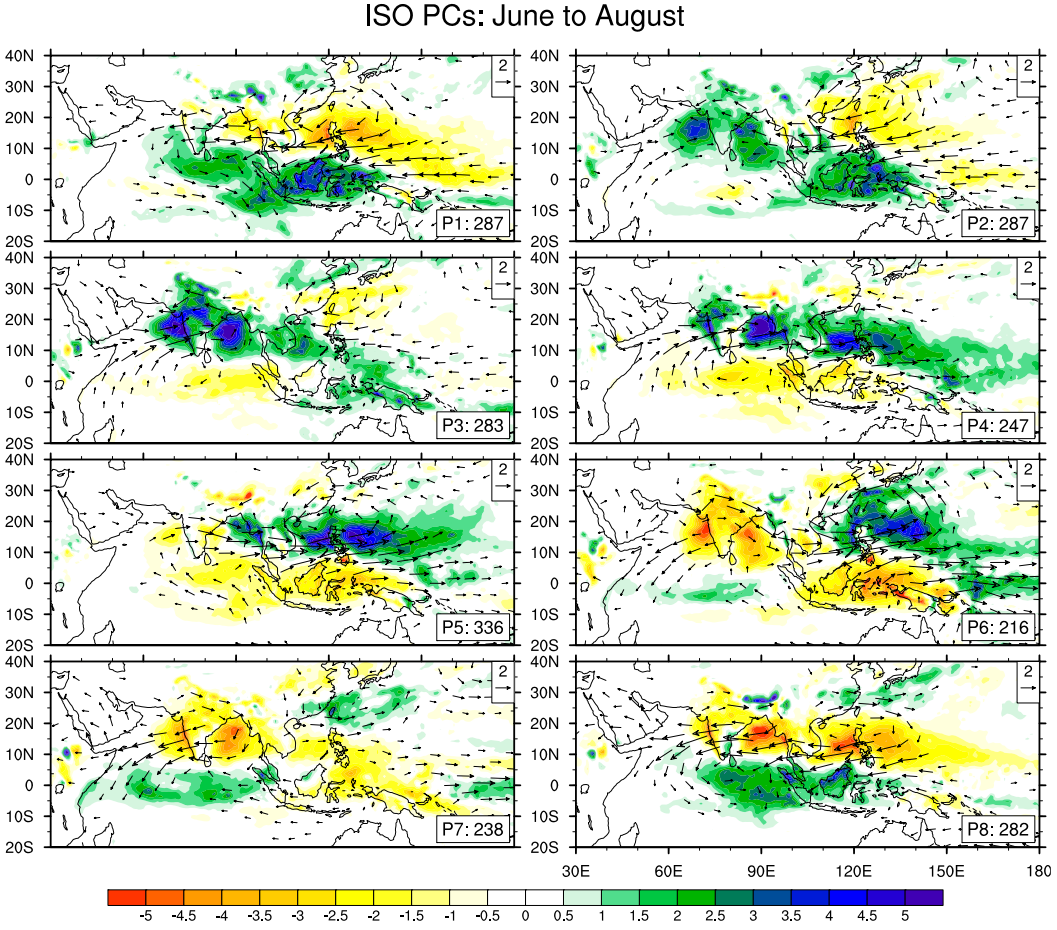

FIG. 4. The life cycle composite of rainfall (shading) and 850-hPa wind (vectors) anomalies reconstructed based on the 20-day low-pass filtered PC_1^{ISO} and PC_2^{ISO}. Wind speed less than 0.3 m s^{-1} is omitted. The number shown in the bottom-right corner is the total days in each phase.

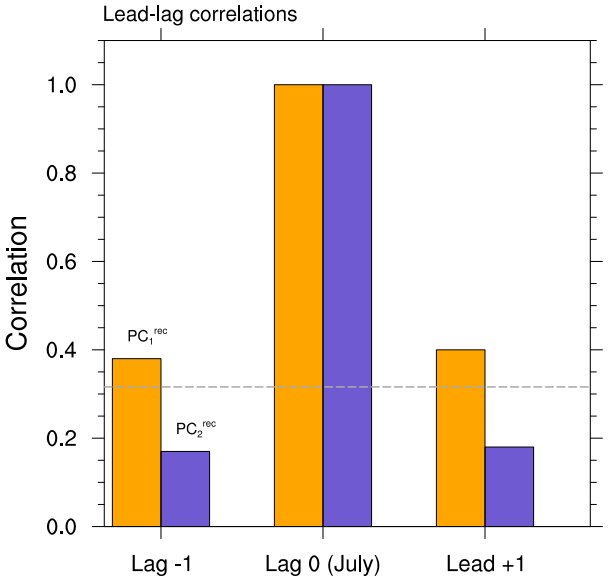

FIG. 5. The 1-month lead–lag autocorrelations of the interannual $PC_{1,2}^{rec}$. Lag 0 represents the autocorrelations of the interannual $PC_{1,2}^{rec}$ in July, lag −1 for July and June, and lead +1 for July and August. Gray dashed line shows the 95% significance level, based on the *t* test.

anomalies are strikingly similar: in El Niño summer, an anomalous cyclonic circulation develops over the South China Sea to NWP whereas in post–El Niño summer it is replaced with an AAC. The spatial correlation of EOF_1^{rec} for low-level zonal wind anomalies in the NWP domain (5°–35°N, 110°–150°E) is −0.9 with the El Niño summer pattern and 0.97 with the post–El Niño summer pattern known as the IPOC (Xie et al. 2016). This indicates that the NWP-AAC has a tendency of a biennial oscillation for the phase reversal from one year to the next. The rainfall anomaly pattern is not as similar: there is a zonal dipole between the equatorial Pacific and Maritime Continent in El Niño summer as opposed to marked rainfall decrease over the NWP in post–El Niño summer that forms a positive feedback with the AAC—the decreased convective heating in the off-equatorial NWP induces the AAC as the Rossby wave response while the subsidence in the AAC suppresses deep convection. While it is reconstructed from the ISO modes, the NWP-AAC is related to both the concurrent and antecedent ENSO conditions. The ISO phases 2 and 6 (Fig. 4) resemble the interannual NWP-AAC (Fig. 2c), further suggesting connections between the ISO and interannual variability through the NWP-AAC pattern in the summer Indo–NWP region.

We use the 20–100-day bandpass filtered data to repeat the same EOF analyses following Eqs. (6) and (7). The NWP-AAC is still the reconstructed leading interannual mode (not shown). Indeed, our previous study (X. Wang et al. 2020) suggested that the interannual NWP-AAC variability partially arises from ISO. It is remarkable that the NWP-AAC emerges as the common pattern for ISO, ENSO, and post-ENSO summer anomalies. Marked zonal wind anomalies over the broad confluence zone between the mean monsoon westerlies and easterly trades from the South China Sea to NWP are indicative of conversion of mean to eddy kinetic.

The EOF_2^{rec} mode accounts for 39.6% of combined reconstructed upper and low-level wind variance with increased ISM rainfall (Fig. 2d), representing ISO contributions to ISM interannual variability (Goswami and Xavier 2005). Of reduced variance compared to the EOF_1^{rec}, EOF_2^{rec} is an atmospheric internal mode with weak temporal persistence (Fig. 5).

c. NWP-AAC as the base mode of ISO

The first two ISO modes (PC_1^{ISO} and PC_2^{ISO}) explain about equal variance, suggesting that their choice as base functions of ISO is arbitrary, statistically not different from any base functions by rotating Cartesian coordinates. Specifically, one can choose the PC_1^{rec} (NWP-AAC mode) and PC_2^{rec} as base functions. The time series of intraseasonal (daily) NWP-AAC and its orthogonal mode are defined by rotating the first two ISO modes by an angle θ:

$$PC_{NWP\text{-}AAC} = PC_1^{rec} = \cos\theta \times PC_1^{ISO} + \sin\theta \times PC_2^{ISO} \quad (8)$$

and

$$PC_2^{rec} = \cos\theta \times PC_2^{ISO} - \sin\theta \times PC_1^{ISO}. \quad (9)$$

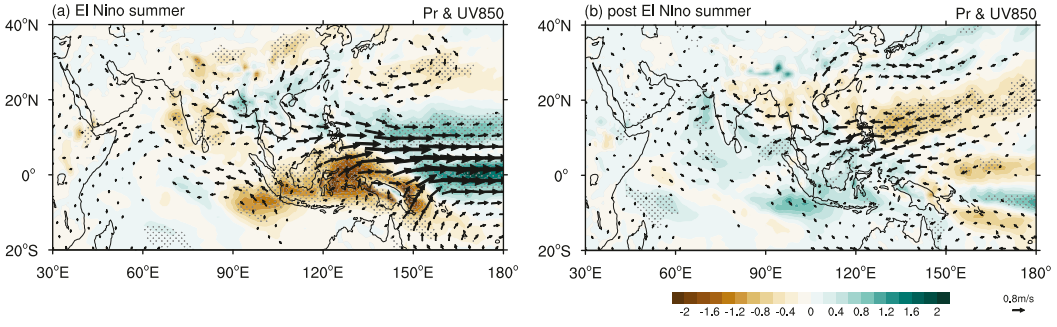

FIG. 6. Rainfall (shading) and 850-hPa wind (vectors) anomalies in (a) El Niño summer and (b) post–El Niño summer, obtained by regressing against subsequent and antecedent DJF Niño-3.4 SST. Stippling represents the rainfall anomalies > 99% confidence level, based upon the *t* test.

Here, $\theta = \tan^{-1} r_2/r_1$, $r_1 = \mathrm{Corr}(\mathrm{PC}_1^{\mathrm{rec}}, \overline{\mathrm{PC}_1^{\mathrm{ISO}}})$, and $r_2 = \mathrm{Corr}(\mathrm{PC}_1^{\mathrm{rec}}, \overline{\mathrm{PC}_2^{\mathrm{ISO}}})$ are the correlation coefficients of the interannual (monthly) NWP-AAC mode $\mathrm{PC}_1^{\mathrm{rec}}$ with the monthly averaged $\mathrm{PC}_1^{\mathrm{ISO}}$ and $\mathrm{PC}_2^{\mathrm{ISO}}$, respectively (Chen et al. 2017). The rotated EOFs remain spatially orthogonal while the daily PCs temporally orthogonal. Using Eqs. (8) and (9), the angle θ of rotation from $\mathrm{PC}_{1,2}^{\mathrm{ISO}}$ to $\mathrm{PC}_{1,2}^{\mathrm{rec}}$ is 47°.

Figure 7 compares the spectra and cross-coherence of the daily $\mathrm{PC}_{1,2}^{\mathrm{rec}}$ pair and the daily $\mathrm{PC}_{1,2}^{\mathrm{ISO}}$ pair Like the $\mathrm{PC}_{1,2}^{\mathrm{ISO}}$ pair, the cross-coherence between $\mathrm{PC}_1^{\mathrm{rec}}$ and $\mathrm{PC}_2^{\mathrm{rec}}$ peaks on the intraseasonal time scale at 90° phase difference, but it nearly vanishes on the interannual time scale. The power spectrum of daily $\mathrm{PC}_1^{\mathrm{rec}}$ peaks on both intraseasonal and interannual time scales while that of $\mathrm{PC}_2^{\mathrm{rec}}$ is low and white on the interannual time scale. We rotate the $\mathrm{PC}_{1,2}^{\mathrm{ISO}}$ by other angles, and the interannual cross-coherence vanishes only at the angle of $\mathrm{PC}_{1,2}^{\mathrm{rec}}$. This indicates that the NWP-AAC mode $\mathrm{EOF}_1^{\mathrm{rec}}$ is a common base function for both ISO and interannual variability while $\mathrm{EOF}_2^{\mathrm{rec}}$ is unique to ISO. On the interannual time scale, the NWP-AAC mode is anchored by large-scale SST anomalies (e.g., over the tropical Indian Ocean) and hence gains month-to-month persistence (Fig. 5). The NWP-AAC spectrum peaks around 180 days, corresponding to the biennial frequency in the concatenated daily time series for JJA. This is consistent with the biennial tendency of the NWP-AAC induced by ENSO (Fig. 6).

The contrast between 1997 and 1998 summers illustrates the biennial tendency. In the summer of 1998 (Fig. S1 in the online supplemental material) that follows a major El Niño, major flooding of the Yangtze River devastated central eastern China. Because of strongly suppressed convection (Fig. 2c), the first NWP typhoon (Nichole) did not form until 9 July. It set the record in the late start of the NWP typhoon season. In comparison, 1997 saw six typhoons before August. Interestingly, the evolution of 1998 summer in ISO phase space is solely distributed along the positive $\mathrm{PC}_1^{\mathrm{rec}}$ axis and averages out nearly zero on the orthogonal axis $\mathrm{PC}_2^{\mathrm{rec}}$.

d. Energetics of the NWP-AAC mode

It is not by accident that the NWP-AAC mode is active across intraseasonal to interannual time scales as it is energized by barotropic energy conversion and convective feedback as this subsection shows. Thus, the NWP-AAC mode is an intrinsic fundamental mode set by the summer mean state of Indo–NWP climate and the zonal wind confluence in particular. The next subsection further shows that the mean state further enables this mode to evolve into coherent ISO with northeastward phase propagation.

The interannual NWP-AAC mode (Fig. 2c) displays the largest variance in the NWP, especially within the low-level confluence zone, which is different from the ISO1 or ISO2 (Figs. 2a and 2b). The total upper- and low-level wind variance explained by the NWP-AAC is 1.5 times larger than the second interannual mode $\mathrm{EOF}_2^{\mathrm{rec}}$. The NWP-AAC is related to ENSO events and shows significant temporal persistence while the $\mathrm{EOF}_2^{\mathrm{rec}}$ does not. This suggests that the interannual NWP-AAC might be a fundamental mode due to the mean state. The change in spatial pattern from ISO (Figs. 2a and 2b) to the interannual

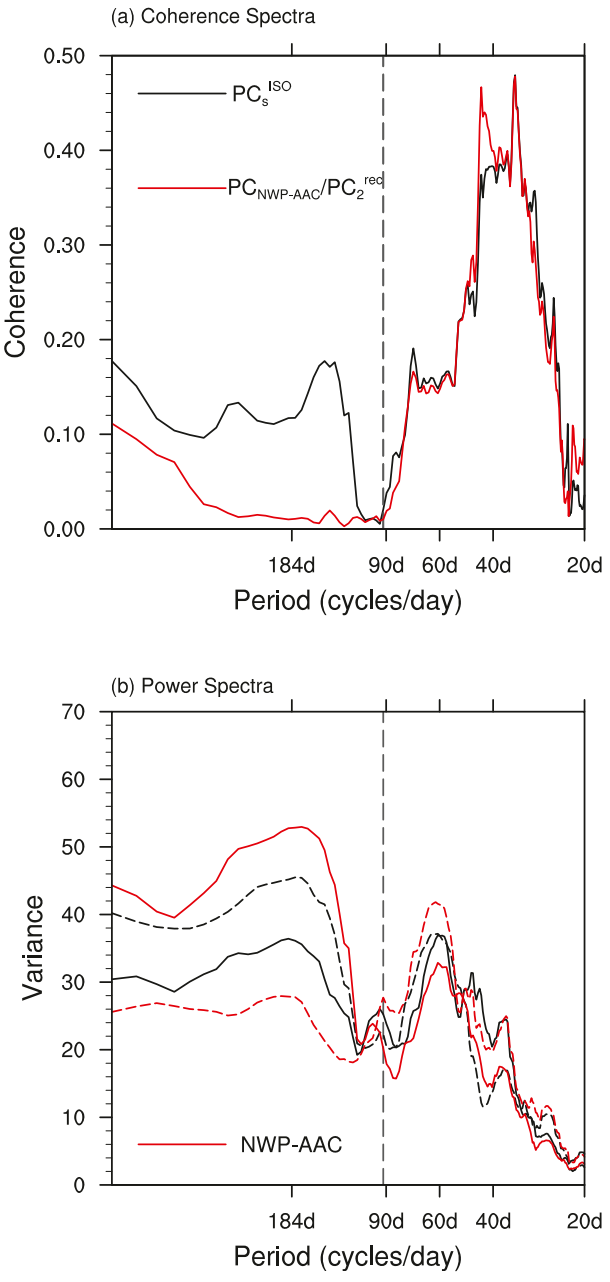

FIG. 7. (a) Coherence spectra of $\mathrm{PC}_1^{\mathrm{ISO}}$ with $\mathrm{PC}_2^{\mathrm{ISO}}$ (black line) and of $\mathrm{PC}_1^{\mathrm{rec}}$ with $\mathrm{PC}_2^{\mathrm{rec}}$ (red line). (b) Power spectra of $\mathrm{PC}_1^{\mathrm{ISO}}$ (black solid line), $\mathrm{PC}_2^{\mathrm{ISO}}$ (black dashed line), $\mathrm{PC}_{\mathrm{NWP\text{-}AAC}}$ (red solid line), and $\mathrm{PC}_2^{\mathrm{rec}}$ (red dashed line).

modes (Figs. 2c and 2d) might be caused by the differences in the barotropic and baroclinic energy conversions.

The governing equation for total eddy energy is presented in section 2b. Here we present results from energetics analysis for the interannual NWP-AAC mode. Large positive barotropic conversion CK is on the south flank of the NWP-AAC within the confluence zone between the mean monsoon westerlies and easterly trade winds (Fig. 8a), where $-\partial\overline{u}/\partial x > 0$ (Hu et al. 2019; X. Wang et al. 2020). In other words, in the confluence

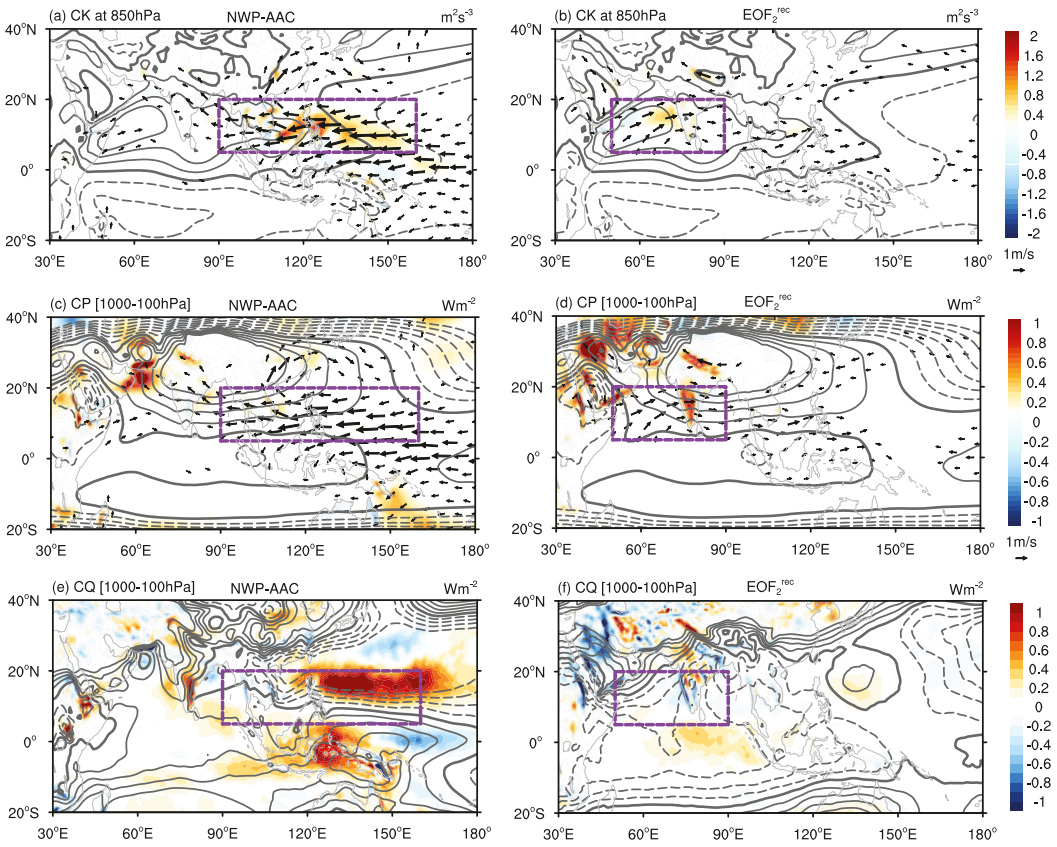

FIG. 8. Horizontal distributions of (a) barotropic energy conversion CK ($\times 10^{-5}\,m^2\,s^{-3}$; shading) at 850 hPa, (c) baroclinic energy conversion CP, and (e) diabatic APE generation CQ integrated vertically from the surface to the 100 hPa level ($\times 10^{-2}\,W\,m^{-2}$; shading) regressed onto the PC of interannual NWP-AAC mode. (b),(d),(f) As in (a), (c), and (e), but regressed onto the second interannual EOF PC_2^{rec}. Contours in (a) and (b) represent the climatological zonal wind at 850 hPa (at intervals of $4\,m\,s^{-1}$ from -4 to $12\,m\,s^{-1}$). The dashed contours in (a) and (b) indicate the easterlies. Contours in (c) and (d) denote the climatological temperature at 500 hPa (at intervals of 0.5 K). The dashed contours in (c) and (d) represent temperature less than 268 K. Contours in (e) and (f) indicate the vertically integrated tropospheric temperature anomalies from the surface to 100 hPa regressed onto the NWP-AAC and EOF_2^{rec} (at intervals of 20 K from -80 to 80 K). Solid and dashed lines in (e) and (f) represent the positive and negative anomalies, respectively. Vectors in (a)–(d) denote the wind anomalies at 850 hPa regressed onto each mode. Purple rectangles show the area for calculating the replenishment timescale τ.

zone, the advection by the mean zonal wind $-(u'^2/2)(\partial\overline{u}/\partial x)$ reinforces the zonal wind anomalies, whereas other terms of CK in Eq. (3) are much smaller (not shown). To measure the efficiency of CK in maintaining the low-level easterly wind anomalies on the southern flank of the NWP-AAC, we evaluate the timescale $\tau_{CK} \equiv \langle KE\rangle/\langle CK\rangle$, where the angle bracket represents area mean over the mean confluence zone of 5°–20°N, 90°–160°E. The value of τ_{CK} denotes how long it takes for the local eddy kinetic energy to be replenished through CK (Kosaka and Nakamura 2006). The sign of the time scale indicates the net energy gain (positive) or loss (negative) for the perturbation. For the NWP-AAC, τ_{CK} is 3.5 days, indicating the importance of the barotropic energy conversion for the mode.

In the tropics, tropospheric temperature perturbations are weak, and the vertically integrated baroclinic conversion CP related to the NWP-AAC is generally small (Fig. 8c). We evaluate the time scale $\tau_{CP} \equiv \langle APE\rangle/\langle CP\rangle$ of the column integral, which presents how long it takes for the eddy available potential energy (APE) to be fully replenished through CP. Over 5°–20°N, 90°–160°E, τ_{CP} is -16.7 days, suggesting that the atmospheric baroclinic energy conversion CP is small and acts to damp the NWP-AAC.

In the tropics, the moist process is very important. The vertically integrated diabatic heating CQ associated with the NWP-AAC is positive over the Maritime Continent and the NWP, where major centers of precipitation anomalies are located (Figs. 2c and 8e). We evaluate the time scale $\tau_{CQ} \equiv \langle APE\rangle/\langle CQ\rangle$, which denotes the time scale of convective feedback. In the mean confluence zone of the NWP, τ_{CQ} is 1 day, suggesting a strong convective feedback for the NWP-AAC mode. In Eq. (4), the CQ term appears as a forcing for the NWP-AAC, but the anomalous circulation can also affect convective activities associated with the NWP-AAC through

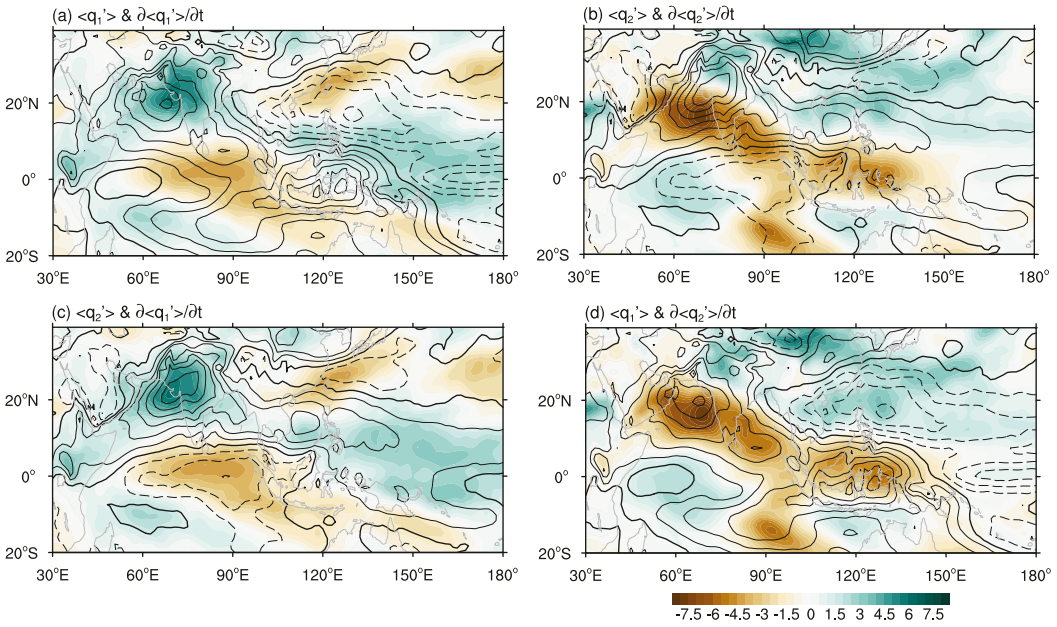

FIG. 9. Vertically integrated moisture anomalies $\langle q' \rangle$ (contours) and the time tendency $\partial\langle q' \rangle/\partial t$ (shading): (a) $\langle q_1' \rangle$ and $\partial\langle q_1' \rangle/\partial t$, (b) $\langle q_2' \rangle$ and $\partial\langle q_2' \rangle/\partial t$, (c) $\langle q_2' \rangle$ and $\partial\langle q_1' \rangle/\partial t$, and (d) $\langle q_1' \rangle$ and $\partial\langle q_2' \rangle/\partial t$. Here $\langle q_1' \rangle$ is the regression against the intraseasonal $PC_{NWP\text{-}AAC}$ and $\langle q_2' \rangle$ is the regression against the intraseasonal PC_2^{rec}.

anomalous vertical motion, moisture advection and static stability (Kosaka and Nakamura 2006, 2010). Thus, the CQ term should be treated as a positive feedback between anomalous circulation and convection associated with the NWP-AAC. While convective feedback is possible over the broad warm pool–Asian monsoon region, the selection of the specific NWP-AAC pattern as the preferred cross-scale mode in the region is due mostly to the barotropic energy conversion in the NWP confluence zone (Fig. 8a).

For EOF_2^{rec}, CK is positive west of India but small in magnitude (Fig. 8b), indicating some contribution of barotropic energy conversion to the ISM interannual variability (Suhas et al. 2012). Over 5°–20°N, 50°–90°E, low-level wind anomalies of the EOF_2^{rec} are weak with $\tau_{CK} = -1.2$ days, representing a damping effect. For EOF_2^{rec}, CP is positive over India and the foothills of the Himalayas (Fig. 8d), but τ_{CP} is negative over the ISM region. CQ is negligible for the EOF_2^{rec} (Fig. 8f).

e. *Northeastward propagation of ISO*

Here, we investigate the phase propagation of ISO from the intraseasonal NWP-AAC perspective, instead of the traditional pair of the ISO1 and ISO2 modes. Figure 9a shows the column-integrated moisture anomalies $\langle q_1' \rangle$ and the corresponding moisture tendency $\partial\langle q_1' \rangle/\partial t$ regressed onto the intraseasonal PC_1^{rec}. The distribution of column-integrated moisture is in phase with the precipitation distribution for the intraseasonal NWP-AAC (Fig. S2; spatial correlation $r = 0.78$ over 10°S–30°N, 50°–170°E), indicative of strong coherence between water vapor and precipitation over deep convective regions (Bretherton et al. 2004; Muller et al. 2009; Kiranmayi and Maloney 2011; Yasunaga et al. 2019). The western Arabian Sea is an exception, where low SSTs prevent moisture anomalies from causing precipitation change. The consistency between moisture and rainfall in the summer ISO is in accordance with the moisture mode theory, justifying the use of column-integrated moisture anomalies for investigating the mechanisms of summer ISO phase propagation (Sobel and Maloney 2012, 2013; Adames and Kim 2016; Jiang et al. 2018).

The enhanced moisture $\langle q_1' \rangle$ is located in the Maritime Continent and eastern Arabian Sea while the decreased moisture is over the NWP (Fig. 9a). A large positive moisture tendency $\partial\langle q_1' \rangle/\partial t$ north of the enhanced moisture center from India to the western Pacific implies a northeastward movement of ISO convection (Adames et al. 2016; Jiang et al. 2018). A negative moisture tendency is found over the northwestern flank of the NWP-AAC and the equatorial eastern Indian Ocean, resulting in the northward propagation of ISO in the NWP (Mao et al. 2010) and the growth/eastward propagation of a new dry phase over the equatorial Indian Ocean, respectively.

The moisture mode theory is a major conceptual advance in MJO research over the past decade, based on at a perturbation moist static energy (MSE) budget or the column-integrated moisture budget beyond the convective feedback (i.e., the first-order balance between vertical moisture advection and precipitation; Fig. S3a; Sobel and Maloney 2013; Adames and Kim 2016).

The advection of anomalous ISO moisture by the mean monsoon circulation $-\langle \overline{\mathbf{V}} \cdot \nabla q_1' \rangle$ plays an important role for the ISO northeastward propagation (Fig. 10a), especially over the north Indian Ocean. This term is relatively weak in Jiang et al. (2018) but is dominant in Adames et al. (2016) for the ISO propagation. As suggested by Jiang et al. (2018), it may depend on the domain selection and compositing scheme. The advection of mean moisture by the ISO-related circulation $-\langle \mathbf{V}' \cdot \nabla \overline{q} \rangle$ is

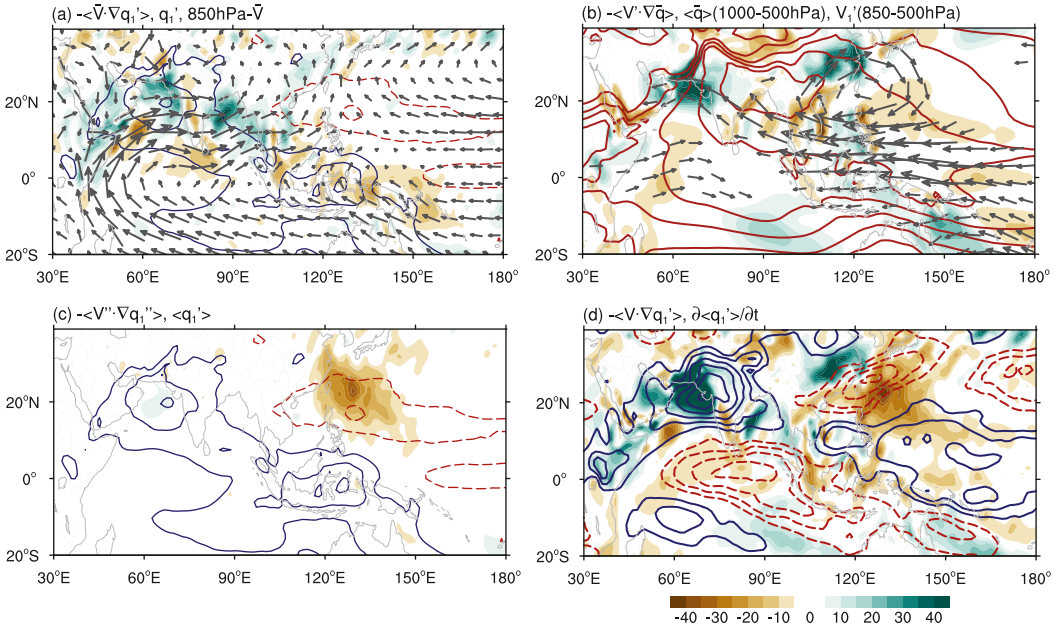

FIG. 10. Vertically integrated horizontal moisture advection terms (shading) regressed onto the intraseasonal $PC_{NWP\text{-}AAC}$: (a) $-\langle\overline{\mathbf{V}}\cdot\nabla q_1'\rangle$, (b) $-\langle\mathbf{V}'\cdot\nabla\overline{q}\rangle$, (c) $-\langle\mathbf{V}''\cdot\nabla q_1''\rangle$, and (d) total horizontal advection term $-\langle\mathbf{V}\cdot\nabla q_1\rangle$. Contours in (a) and (c) represent the vertically integrated moisture anomalies q_1', in (b) indicate climatological 1000–500-hPa integrated specific humidity, and in (d) show the tendency of vertical integrated moisture anomalies $\partial\langle q_1'\rangle/\partial t$. The vector in (a) is the climatological wind at 850 hPa and in (b) is for vertically integrated wind anomalies from 850 to 500 hPa regressed onto the intraseasonal $PC_{NWP\text{-}AAC}$. The zero contour is omitted.

also important for the moisture tendency over the Indian Ocean (Fig. 10b), in accordance with the results of Jiang et al. (2018). The mean moisture peaks over the northern Bay of Bengal (Fig. 10b), and the anomalous zonal wind advection moistens the Arabian Sea while drying the NWP. The advection by higher-frequency disturbances is large in a northwest slanted band toward Taiwan (Fig. 10c); the synoptic disturbances themselves grow in part on the barotropic energy conversion in the mean confluence zone (Lau and Lau 1992; Sobel and Bretherton 1999). The total horizontal advection term $-\langle\mathbf{V}\cdot\nabla q_1\rangle$ (Fig. 10d) is favorable for the northeastward propagation of summer ISO in the Indian Ocean and northward in the NWP. In addition, wind-induced evaporation contributes to the eastward propagation over the equatorial Pacific (Fig. S3b).

The net effect of vertical advection, condensation, and evaporation, which are referred to as the ''column processes'' (Wolding and Maloney 2015), contributes constructively to the tendency $\partial\langle q_1'\rangle/\partial t$, specifically the northward propagation of ISO over the NWP and eastward propagation over the equatorial western Pacific (Adames et al. 2016; Fig. S3c). Large residuals exist in the column-integrated water vapor budget Eq. (4), possibly due to ERA-Interim biases in representing precipitation (not shown; Mapes and Bacmeister 2012; Adames and Wallace 2015).

The column-integrated moisture anomalies $\langle q_2'\rangle$ related to PC_2^{rec} show enhanced convection over India, Bay of Bengal to the equatorial western Pacific with suppressed convection over the equatorial eastern Indian Ocean (Fig. 9b). Figure 9c shows the anomalous moisture tendency $\partial\langle q_1'\rangle/\partial t$ regressed against the intraseasonal PC_2^{rec}, superimposed on the moisture anomalies $\langle q_2'\rangle$ of PC_2^{rec} regressed onto the intraseasonal PC_1^{rec}. The tendency $\partial\langle q_1'\rangle/\partial t$ is in phase with the $\langle q_2'\rangle$ anomalies (spatial correlation $r = 0.79$ over 10°S–30°N, 50°–170°E), suggesting that the ISO evolves from the NWP-AAC mode to its orthogonal mode EOF_2^{rec}. Meanwhile, $\partial\langle q_2'\rangle/\partial t$ is nearly 180° out of phase with the $\langle q_1'\rangle$ (spatial correlation $r = -0.75$ over 10°S–30°N, 50°–170°E). This out-of-phase relationship represents a 90° phase lag between the NWP-AAC and second mode, consistent with the spectral analyses. The pair of PC_1^{rec} and PC_2^{rec} well captures the northward propagation of summer ISO.

4. Summary and discussion

We have identified from observations the anomalous anticyclonic circulation at low levels over the South China Sea to the northwest Pacific as a fundamental mode common to intraseasonal to interannual variability in the region during the boreal summer (JJA). Accompanied by reduced rainfall, this NWP AAC is anchored in the broad confluence zone between the mean monsoon southwesterlies and easterly trades, energized by the resultant barotropic energy conversion and convective feedback (Fig. 11). On the interannual time scale, the NWP-AAC displays a tendency of biennial phase reversal, from cyclonic in El Niño summer to anticyclonic in post–El Niño summer. On the intraseasonal time scale, the mean circulation and moisture distribution are such that the NWP-AAC—equivalent to ISO phase 2 or 6—induces the moisture tendency for the

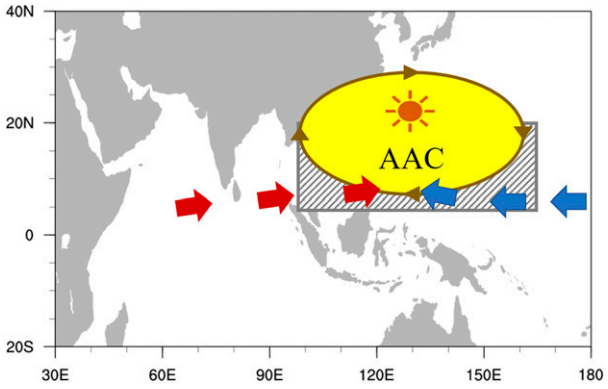

FIG. 11. Schematic for the structure and dynamics of the NWP-AAC mode (the ellipse with arrows). The gray hatched box denotes the mean low-level wind confluence zone between the monsoon westerlies (red box arrows) and easterly trades (blue box arrows).

observed northeast phase propagation over the Asian summer monsoon region. The NWP-AAC is remarkably versatile, excited by distinct SST forcing of the equatorial Pacific in ENSO summers and of the tropical Indo–NWP in post-ENSO summers. Being an unstable mode of the mean Asian summer monsoon system, it plays an important role in shaping the spatiotemporal structure of the ISO. Because of the diverse forcing mechanisms, it is not surprising that anomaly patterns, while resembling the NWP-AAC, differ somewhat among ISO, ENSO, and post-ENSO summers, especially outside the mean flow confluence where barotropic energy conversion takes place.

The NWP-AAC affects summer rainfall over India and eastern China (Fig. 2c) as well as modulating regional typhoon activity (Choi et al. 2010; Du et al. 2011). For eastern China, the moisture transport by the anomalous southwesterlies on the northwestern flank of the AAC often causes heavy rainfall and flooding along the Yangtze River as in the post–El Niño summer of 1998. The historic Yangtze flooding of 2020 summer shows that the range of forcing for NWP-AAC is even wider than thought. In the absence of strong ENSO, the AAC is forced by a strong IOD in autumn 2019, mediated by the south Indian Ocean Rossby waves (Zhou et al. 2021).

The skill of current subseasonal to seasonal forecast may be in part limited by model errors in simulating the rainfall distribution and hence the mean confluence zone on which the NWP-AAC mode is dependent. Climatological deep convection over the tropical NWP starts too early in climate models (Zhou et al. 2016), displacing the mean confluence zone eastward. The erroneous displacement of the AAC pattern away from India and eastern China could reduce the impact in model prediction on these population centers. Summer climatology differs markedly among models over the NWP. Remarkably the intermodel variability seems to project onto the AAC pattern (Kosaka and Nakamura 2011). Besides, the subseasonal to seasonal predictability of the Asian summer monsoon is correlated with ENSO and ISO. Generally, the subseasonal forecast skill of the Asian summer monsoon is only 1–2 weeks and relies on the ISO phases. The predictive skill could exceed 4 weeks during MJO phases 6–7, when ISO convection is enhanced over the NWP (Jie et al. 2017; Vigaud et al. 2017). Our results relate the cross-scale AAC variability to the climatological confluence zone, suggesting that a realistic simulation of the mean Asian summer monsoon can lead to improved subseasonal to seasonal forecast in the region.

Acknowledgments. X. W. and Z. G. are supported by the National Key R&D Program of China (2019YFC1510201), and X. W. is also supported by the China Scholarship Council (201708320296). S.-P. X. is supported by the U.S. National Science Foundation (AGS 1637450).

REFERENCES

Adames, Á. F., and J. M. Wallace, 2015: Three-dimensional structure and evolution of the moisture field in the MJO. *J. Atmos. Sci.*, **72**, 3733–3754, https://doi.org/10.1175/JAS-D-15-0003.1.

——, and D. Kim, 2016: The MJO as a dispersive, convectively coupled moisture wave: Theory and observations. *J. Atmos. Sci.*, **73**, 913–941, https://doi.org/10.1175/JAS-D-15-0170.1.

——, J. M. Wallace, and J. M. Monteiro, 2016: Seasonality of the structure and propagation characteristics of the MJO. *J. Atmos. Sci.*, **73**, 3511–3526, https://doi.org/10.1175/JAS-D-15-0232.1.

Annamalai, H., and J. M. Slingo, 2001: Active/break cycles: Diagnosis of the intraseasonal variability of the Asian summer monsoon. *Climate Dyn.*, **18**, 85–102, https://doi.org/10.1007/s003820100161.

Bretherton, C. S., M. E. Peters, and L. E. Back, 2004: Relationships between water vapor path and precipitation over the tropical oceans. *J. Climate*, **17**, 1517–1528, https://doi.org/10.1175/1520-0442(2004)017<1517:RBWVPA>2.0.CO;2.

Chen, X., J. M. Wallace, and K. K. Tung, 2017: Pairwise-rotated EOFs of global SST. *J. Climate*, **30**, 5473–5489, https://doi.org/10.1175/JCLI-D-16-0786.1.

Choi, K.-S., C.-C. Wu, and E.-J. Cha, 2010: Change of tropical cyclone activity by Pacific–Japan teleconnection pattern in the western North Pacific. *J. Geophys. Res.*, **115**, D19114, https://doi.org/10.1029/2010JD013866.

Dee, D. P., and Coauthors, 2011: The ERA-Interim reanalysis: Configuration and performance of the data assimilation system. *Quart. J. Roy. Meteor. Soc.*, **137**, 553–597, https://doi.org/10.1002/qj.828.

Du, Y., L. Yang, and S. P. Xie, 2011: Tropical Indian Ocean influence on northwest Pacific tropical cyclones in summer following strong El Niño. *J. Climate*, **24**, 315–322, https://doi.org/10.1175/2010JCLI3890.1.

Duchon, C. E., 1979: Lanczos filtering in one and two dimensions. *J. Appl. Meteor.*, **18**, 1016–1022, https://doi.org/10.1175/1520-0450(1979)018<1016:LFIOAT>2.0.CO;2.

Frank, W. M., and P. E. Roundy, 2006: The role of tropical waves in tropical cyclogenesis. *Mon. Wea. Rev.*, **134**, 2397–2417, https://doi.org/10.1175/MWR3204.1.

Goswami, B. N., and R. A. Mohan, 2001: Intraseasonal oscillations and interannual variability of the Indian summer monsoon. *J. Climate*, **14**, 1180–1198, https://doi.org/10.1175/1520-0442(2001)014<1180:IOAIVO>2.0.CO;2.

——, and P. K. Xavier, 2005: Dynamics of "internal" interannual variability of the Indian summer monsoon in a GCM. *J. Geophys. Res.*, **110**, D24104, https://doi.org/10.1029/2005JD006042.

Grimm, A. M., 2019: Madden–Julian oscillation impacts on South American summer monsoon season: Precipitation anomalies, extreme events, teleconnections, and role in the MJO cycle. *Climate Dyn.*, **53**, 907–932, https://doi.org/10.1007/s00382-019-04622-6.

Hoskins, B. J., I. N. James, and G. H. White, 1983: The shape, propagation and mean-flow interaction of large-scale weather systems. *J. Atmos. Sci.*, **40**, 1595–1612, https://doi.org/10.1175/1520-0469(1983)040<1595:TSPAMF>2.0.CO;2.

Hu, K., G. Huang, S. P. Xie, and S. M. Long, 2019: Effect of the mean flow on the anomalous anticyclone over the Indo-northwest Pacific in post-El Niño summers. *Climate Dyn.*, **53**, 5725–5741, https://doi.org/10.1007/s00382-019-04893-z.

Jiang, X., and N.-C. Lau, 2008: Intraseasonal teleconnection between North American and western North Pacific monsoons with 20-day time scale. *J. Climate*, **21**, 2664–2679, https://doi.org/10.1175/2007JCLI2024.1.

——, Á. F. Adames, M. Zhao, D. Waliser, and E. Maloney, 2018: A unified moisture mode framework for seasonality of the Madden–Julian oscillation. *J. Climate*, **31**, 4215–4224, https://doi.org/10.1175/JCLI-D-17-0671.1.

Jie, W., F. Vitart, T. Wu, and X. Liu, 2017: Simulations of the Asian summer monsoon in the sub-seasonal to seasonal prediction project (S2S) database. *Quart. J. Roy. Meteor. Soc.*, **143**, 2282–2295, https://doi.org/10.1002/qj.3085.

Joseph, S., A. Sahai, and B. Goswami, 2009: Eastward propagating MJO during boreal summer and Indian monsoon droughts. *Climate Dyn.*, **32**, 1139–1153, https://doi.org/10.1007/s00382-008-0412-8.

Kiranmayi, L., and E. D. Maloney, 2011: Intraseasonal moist static energy budget in reanalysis data. *J. Geophys. Res.*, **116**, D21117, https://doi.org/10.1029/2011JD016031.

Kosaka, Y., and H. Nakamura, 2006: Structure and dynamics of the summertime Pacific–Japan teleconnection pattern. *Quart. J. Roy. Meteor. Soc.*, **132**, 2009–2030, https://doi.org/10.1256/qj.05.204.

——, and ——, 2010: Mechanisms of meridional teleconnection observed between a summer monsoon system and a subtropical anticyclone. Part I: The Pacific–Japan pattern. *J. Climate*, **23**, 5085–5108, https://doi.org/10.1175/2010JCLI3413.1.

——, and ——, 2011: Dominant mode of climate variability, intermodel diversity, and projected future changes over the summertime western North Pacific simulated in the CMIP3 models. *J. Climate*, **24**, 3935–3955, https://doi.org/10.1175/2011JCLI3907.1.

Lau, K.-H., and N.-C. Lau, 1992: The energetics and propagation dynamics of tropical summertime synoptic-scale disturbances. *Mon. Wea. Rev.*, **120**, 2523–2539, https://doi.org/10.1175/1520-0493(1992)120<2523:TEAPDO>2.0.CO;2.

Lee, J. Y., B. Wang, M. C. Wheeler, X. Fu, D. E. Waliser, and I. S. Kang, 2013: Real-time multivariate indices for the boreal summer intraseasonal oscillation over the Asian summer monsoon region. *Climate Dyn.*, **40**, 493–509, https://doi.org/10.1007/s00382-012-1544-4.

Lorenz, D. J., and D. L. Hartmann, 2006: The effect of the MJO on the North American monsoon. *J. Climate*, **19**, 333–343, https://doi.org/10.1175/JCLI3684.1.

Madden, R. A., and P. R. Julian, 1971: Detection of a 40–50 day oscillation in the zonal wind in the tropical Pacific. *J. Atmos. Sci.*, **28**, 702–708, https://doi.org/10.1175/1520-0469(1971)028<0702:DOADOI>2.0.CO;2.

——, and ——, 1972: Description of global-scale circulation cells in the tropics with a 40–50 day period. *J. Atmos. Sci.*, **29**, 1109–1123, https://doi.org/10.1175/1520-0469(1972)029<1109:DOGSCC>2.0.CO;2.

Maloney, E. D., and D. L. Hartmann, 2000: Modulation of eastern North Pacific hurricanes by the Madden–Julian oscillation. *J. Climate*, **13**, 1451–1460, https://doi.org/10.1175/1520-0442(2000)013<1451:MOENPH>2.0.CO;2.

Mao, J., Sun, Z. and Wu, G., 2010: 20–50-day oscillation of summer Yangtze rainfall in response to intraseasonal variations in the subtropical high over the western North Pacific and South China Sea. *Climate Dyn.*, **34**, 747–761, https://doi.org/10.1007/s00382-009-0628-2.

Mapes, B. E., and J. T. Bacmeister, 2012: Diagnosis of tropical biases and the MJO from patterns in the MERRA analysis tendency fields. *J. Climate*, **25**, 6202–6214, https://doi.org/10.1175/JCLI-D-11-00424.1.

McPhaden, M. J., 1999: Genesis and evolution of the 1997–98 El Niño. *Science*, **283**, 950–954, https://doi.org/10.1126/science.283.5404.950.

Mishra, V., B. V. Smoliak, D. P. Lettenmaier, and J. M. Wallace, 2012: A prominent pattern of year-to-year variability in Indian summer monsoon rainfall. *Proc. Natl. Acad. Sci. USA*, **109**, 7213–7217, https://doi.org/10.1073/pnas.1119150109.

Moore, A. M., and R. Kleeman, 1999: Stochastic forcing of ENSO by the intraseasonal oscillation. *J. Climate*, **12**, 1199–1220, https://doi.org/10.1175/1520-0442(1999)012<1199:SFOEBT>2.0.CO;2.

Muller, C. J., L. E. Back, P. A. O'Gorman, and K. A. Emanuel, 2009: A model for the relationship between tropical precipitation and column water vapor. *Geophys. Res. Lett.*, **36**, L16804, https://doi.org/10.1029/2009GL039667.

Pohl, B., and P. Camberlin, 2006: Influence of the Madden–Julian oscillation on East African rainfall. I: Intraseasonal variability and regional dependency. *Quart. J. Roy. Meteor. Soc.*, **132**, 2521–2539, https://doi.org/10.1256/qj.05.104.

Saji, N. H., B. N. Goswami, P. N. Vinayachandran, and T. Yamagata, 1999: A dipole mode in the tropical Indian Ocean. *Nature*, **401**, 360–363, https://doi.org/10.1038/43854.

Small, R. J., S. P. Xie, E. D. Maloney, S. P. de Szoeke, and T. Miyama, 2011: Intraseasonal variability in the far-east Pacific: Investigation of the role of air–sea coupling in a regional coupled model. *Climate Dyn.*, **36**, 867–890, https://doi.org/10.1007/s00382-010-0786-2.

Sobel, A. H., and C. S. Bretherton, 1999: Development of synoptic-scale disturbances over the summertime tropical northwest Pacific. *J. Atmos. Sci.*, **56**, 3106–3127, https://doi.org/10.1175/1520-0469(1999)056<3106:DOSSDO>2.0.CO;2.

——, and E. Maloney, 2012: An idealized semi-empirical framework for modeling the Madden–Julian oscillation. *J. Atmos. Sci.*, **69**, 1691–1705, https://doi.org/10.1175/JAS-D-11-0118.1.

——, and ——, 2013: Moisture modes and the eastward propagation of the MJO. *J. Atmos. Sci.*, **70**, 187–192, https://doi.org/10.1175/JAS-D-12-0189.1.

Suhas, E., J. M. Neena, and B. N. Goswami, 2012: Interannual variability of Indian summer monsoon arising from interactions between seasonal mean and intraseasonal oscillations. *J. Atmos. Sci.*, **69**, 1761–1774, https://doi.org/10.1175/JAS-D-11-0211.1.

Vigaud, N., A. W. Robertson, M. K. Tippett, and N. Acharya, 2017: Subseasonal predictability of boreal summer monsoon rainfall from ensemble forecasts. *Front. Environ. Sci.*, **5**, 67, https://doi.org/10.3389/fenvs.2017.00067.

Wang, B., R. Wu, and T. Li, 2003: Atmosphere–warm ocean interaction and its impacts on Asian–Australian monsoon variation. *J. Climate*, **16**, 1195–1211, https://doi.org/10.1175/1520-0442(2003)16<1195:AOIAII>2.0.CO;2.

Wang, C.-Y., S.-P. Xie, and Y. Kosaka, 2018: Indo-western Pacific climate variability: ENSO forcing and internal dynamics in a tropical Pacific pacemaker simulation. *J. Climate*, **31**, 10 123–10 139, https://doi.org/10.1175/JCLI-D-18-0203.1.

——, ——, and ——, 2020: ENSO-unrelated variability in Indo–northwest Pacific climate: Regional and coupled ocean–atmospheric feedback. *J. Climate*, **33**, 4095–4108, https://doi.org/10.1175/JCLI-D-19-0426.1.

Wang, X., S.-P. Xie, and Z. Guan, 2020: Atmospheric internal variability in the summer Indo–northwestern Pacific: Role of the intraseasonal oscillation. *J. Climate*, **33**, 3395–3410, https://doi.org/10.1175/JCLI-D-19-0794.1.

Webster, P. J., and S. Yang, 1992: Monsoon and ENSO: Selectively interactive systems. *Quart. J. Roy. Meteor. Soc.*, **118**, 877–926, https://doi.org/10.1002/qj.49711850705.

Wheeler, M. C., and H. H. Hendon, 2004: An all-season real-time multivariate MJO index: Development of an index for monitoring and prediction. *Mon. Wea. Rev.*, **132**, 1917–1932, https://doi.org/10.1175/1520-0493(2004)132<1917:AARMMI>2.0.CO;2.

——, ——, S. Cleland, H. Meinke, and A. Donald, 2009: Impacts of the Madden–Julian oscillation on Australian rainfall and circulation. *J. Climate*, **22**, 1482–1498, https://doi.org/10.1175/2008JCLI2595.1.

Wolding, B. O., and E. D. Maloney, 2015: Objective diagnostics and the Madden–Julian oscillation. Part II: Application to moist static energy and moisture budgets. *J. Climate*, **28**, 7786–7808, https://doi.org/10.1175/JCLI-D-14-00689.1.

Wu, B., T. Li, and T. Zhou, 2010: Relative contributions of the Indian Ocean and local SST anomalies to the maintenance of the western North Pacific anomalous anticyclone during the El Niño decaying summer. *J. Climate*, **23**, 2974–2986, https://doi.org/10.1175/2010JCLI3300.1.

Xie, P., and P. A. Arkin, 1997: Global precipitation: A 17-year monthly analysis based on gauge observations, satellite estimates, and numerical model outputs. *Bull. Amer. Meteor. Soc.*, **78**, 2539–2558, https://doi.org/10.1175/1520-0477(1997)078<2539:GPAYMA>2.0.CO;2.

Xie, S.-P., K. Hu, J. Hafner, H. Tokinaga, Y. Du, G. Huang, and T. Sampe, 2009: Indian Ocean capacitor effect on Indo–western Pacific climate during the summer following El Niño. *J. Climate*, **22**, 730–747, https://doi.org/10.1175/2008JCLI2544.1.

——, Y. Kosaka, Y. Du, K. Hu, J. S. Chowdary, and G. Huang, 2016: Indo-western Pacific Ocean capacitor and coherent climate anomalies in post-ENSO summer: A review. *Adv. Atmos. Sci.*, **33**, 411–432, https://doi.org/10.1007/s00376-015-5192-6.

Yasunaga, K., S. Yokoi, K. Inoue, and B. E. Mapes, 2019: Space–time spectral analysis of the moist static energy budget equation. *J. Climate*, **32**, 501–529, https://doi.org/10.1175/JCLI-D-18-0334.1.

Zhang, C., 2013: Madden–Julian oscillation: Bridging weather and climate. *Bull. Amer. Meteor. Soc.*, **94**, 1849–1870, https://doi.org/10.1175/BAMS-D-12-00026.1.

Zhou, W., S.-P. Xie, and Z.-Q. Zhou, 2016: Slow preconditioning for the abrupt convective jump over the northwest Pacific during summer. *J. Climate*, **29**, 8103–8113, https://doi.org/10.1175/JCLI-D-16-0342.1.

Zhou, Z.-Q., S.-P. Xie, G. J. Zhang, and W. Zhou, 2018: Evaluating AMIP skill in simulating interannual variability over the Indo–western Pacific. *J. Climate*, **31**, 2253–2265, https://doi.org/10.1175/JCLI-D-17-0123.1.

——, ——, and R. Zhang, 2019: Variability and predictability of Indian rainfall during the monsoon onset month of June. *Geophys. Res. Lett.*, **46**, 14 782–14 788, https://doi.org/10.1029/2019GL085495.

——, ——, and ——, 2021: Historic Yangtze flooding of 2020 tied to extreme Indian Ocean conditions. *Proc. Natl. Acad. Sci. USA*, **118**, e2022255118, https://doi.org/10.1073/pnas.2022255118.